ACS APPLIED ELECTRONIC MATERIALS

pubs.acs.org/acsaelm Article

Toward a Hardware Spiking Neural Network: Learning and Adaptation with an Environmental Sustainable Polymer Memristor

Stephen H. Foulger,* Yuriy Bandera, Travis Wanless, Igor Luzinov, Olivia Cobb, Michael G. Sehorn, Lubomir Kostal, Jiří Pfleger, and Jarmila Vilčáková

Cite This: https://doi.org/10.1021/acsaelm.6c00615

ABSTRACT: A hybrid conjugated polymer is presented that supports spike-timing-dependent plasticity (STDP) for neuromorphic computing devices while enabling environmental sustainability through biodegradability. The polymer, distinguished by its carbazole backbone and electrically responsive pendant carbazole groups, forms a two-terminal device that exhibits analog STDP behavior. Demonstrations focus on fundamental switching characteristics using individual devices, offering insights relevant to temporal learning tasks such as speech and image recognition. The energy cost per programming event is 60 nJ. Biodegradation is demonstrated using *Pseudomonas resinovorans* CA10 lysate, supporting reduced electronic waste. This work introduces a sustainable soft-matter platform for synaptic device development.

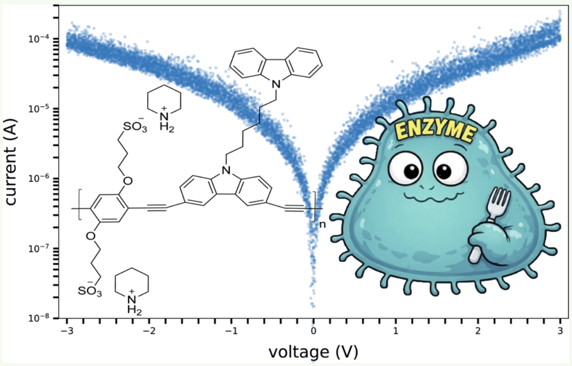

KEYWORDS: *spike-timing-dependent plasticity, neuromorphic computing, biodegradable electronics, polymeric memristor, percolation networks, carbazole, analog switching*

INTRODUCTION

A hardware spiking neural network (SNN) is a type of neuromorphic computing system designed to simulate biological neural networks.[1] Unlike classical von Neumann architectures, which rely on sequential instruction execution, SNNs perform computations through the parallel processing of spikes, discrete events representing the activation of individual neurons. Hardware SNNs typically consist of multiple processing units, each emulating one or more neurons and synapses.[2] These units interconnect to form a network capable of executing complex computations via the interactions of individual neurons and synapses.

Artificial neurons generate spike signals when the input from synapses exceeds a specific threshold. A threshold function evaluates whether sufficient signals have accumulated, mirroring the firing process of biological neurons. Similar to their biological counterparts, most artificial neurons receive current inputs from preceding synapses and produce voltage outputs to subsequent synapses in the form of spikes.

Artificial synapses are engineered to emulate the function of biological synapses, specialized junctions facilitating communication between neurons. Their primary role is to store the strength of connections between artificial neurons and modulate these connections through mechanisms analogous to synaptic plasticity observed in biological systems, such as Hebbian learning or spike-timing-dependent plasticity (STDP).[3] Notable examples include IBM's TrueNorth[4] and Intel's Loihi,[5] both of which are event-driven neuromorphic chips utilizing simulated STDP.

In neuromorphic engineering, artificial synapses are crucial for developing architectures that emulate the complexities of biological neural networks. Current research aims to create artificial synapses that are energy-efficient, scalable, and biologically realistic.[6,7] Two-terminal memristors have become pivotal components in artificial synapses due to their low power consumption, high packing density, and ability to mimic synaptic plasticity. Their architecture, featuring an input and an output terminal, is particularly well-suited for replicating the core functionalities of biological synapses.[7]

Organic and polymeric memristors, among two-terminal memristors, have attracted significant research interest because of their compatibility with mass production techniques such as printing and their adaptability to flexible and nonconformal substrates.[8,9] Most efforts to create two-terminal polymeric memristors have adopted a one-dimensional percolation approach, transitioning an insulating polymer or composite

Received: March 27, 2026
Revised: April 1, 2026
Accepted: April 2, 2026

to a conductive state by dynamically generating a second conductive phase until a percolation threshold is crossed.[10] However, this insulator-to-conductor transition often results in a binary, abrupt switch between states, requiring relatively high voltage pulses and corresponding energy consumption. This limitation suggests the need for further exploration to meet the energy efficiency requirements for practical applications.

To achieve energy-efficient synaptic modulation, investigating memristors that offer an analog response with a broad spectrum of resistive states is a viable approach. Operating in such an analog regime allows conductivity to be smoothly modified across orders of magnitude through subtle adjustments in the percolation network, particularly in the postpercolation region where scaling relationships are maintained.[11]

To realize this objective, we introduce a novel hybrid conjugated polymer endowed with pendant heterocyclic rings, specifically, a copolymer that incorporates a conjugated backbone alongside pendant carbazole moieties. The unique architecture of this polymer, combining a conductive backbone with electroactive ligands, provides dual, synergistic pathways to establish the percolation network.[12−14]

By leveraging these two independent but complementary routes, we can finely control the percolation network, achieving a wider range of resistive states through low-energy modifications. This innovation not only paves the way for more energy-efficient artificial synapses but also opens new avenues for utilizing advanced polymeric materials in neuromorphic applications. The structure of the repeat unit of the polymer used in this study is presented in Figure 1, obtained by a Sonogashira coupling reaction between sodium 3,3′-((2,5-diiodo-1,4-phenylene)bis(oxy))bis(propane-1-sulfonate) and 9-(6-(9*H*-carbazol-9-yl)hexyl)-3,6-diethynyl-9*H*-carbazole, and is referred to as pB6CC.[15,16] This dual mechanism benefits from the intrinsic charge transport properties of the conjugated backbone and the electroactive of the pendant carbazole groups.

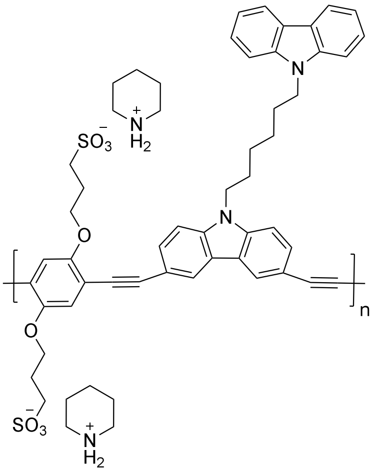

Figure 1. Polymer repeat unit (pB6CC) composed of piperidinium 3,3′-(1,4-phenylenebis(oxy))bis(propane-1-sulfonate) and 9-[6-(9-carbazolyl)hexyl]-3,6-diethynylcarbazole.

In existing literature, both nonconjugated[17−21] and conjugated[22−25] polymers have utilized pendant carbazole moieties that are sensitive to external electric fields, resulting in memristors with bistable switching behavior. In our system, the baseline conductivity is established through the conjugated phenyl/carbazole backbone, forming a static percolating network that serves as the primary charge transport channel. Meanwhile, the electroactive pendant carbazole moieties, covalently attached to the backbone, provide a dynamic percolation mechanism. These carbazole units can undergo conformational rearrangements to create additional conductive pathways.

The dynamism introduced by this second percolation mechanism, facilitated by the carbazole groups, modulates the redundancy within the overall percolation network, resulting in a broad spectrum of resistive states. This allows for more nuanced control of electrical properties.[14] Therefore, our system uniquely integrates two independent yet synergistic pathways to achieve a continuum of resistive states, promising applications that require low-energy, analog switching behavior.

Additionally, the incorporation of carbazole into this synthetic polymer was carefully selected to optimize both charge transport characteristics and to serve as a substrate for *Pseudomonas resinovorans CA10*. The unique inclusion of carbazole not only enhances electrical conductivity and facilitates efficient charge transport, critical for high-performance memristive operations, but also provides specific binding sites essential for targeted enzymatic degradation. This dual functionality makes carbazole an integral component in achieving both superior device performance and controlled biodegradability. Unlike previously reported biodegradable memristors based on biomolecules,[26−29] nonbiodegradable components on a biodegradable substrate,[30] or water-soluble polymers such as PVA,[31] our system employs a high-performance synthetic polymer specifically degraded by a specialized bacterium. This targeted degradation pathway ensures efficient and predictable polymer breakdown in the presence of *Pseudomonas resinovorans CA10*, addressing environmental sustainability without compromising the device's operational integrity. Furthermore, the synthetic nature of the polymer allows for precise molecular engineering, enabling fine-tuning of electronic properties and degradation rates, which is not feasible with naturally derived biomolecules. This combination of high electrical performance, specific biodegradation, and molecular tunability distinguishes our memristor from existing biodegradable technologies, positioning it as a pioneering solution in sustainable neuromorphic computing devices.

■ RESULTS AND DISCUSSION

The memristive devices investigated in this work consist of an ITO/pB6CC/Al structure fabricated as described in the Experimental Section, where thin films of the pB6CC polymer were deposited by spin coating from a 1:1 water/tetrahydrofuran solution (10 mg/mL) onto patterned ITO substrates, followed by thermal evaporation of the top aluminum electrode. The morphology of the resulting polymer films was examined using scanning electron microscopy (SEM), as shown in Figure 2. The SEM images reveal a continuous polymer film exhibiting a nanoscale granular texture with no evidence of macroscopic pinholes or large structural discontinuities. The granular morphology appears uniform across several microns, indicating that the spin-coating process produces a well-formed thin film on the ITO electrode. Such nanoscale structural heterogeneity is consistent with the formation of distributed conduction pathways that can support

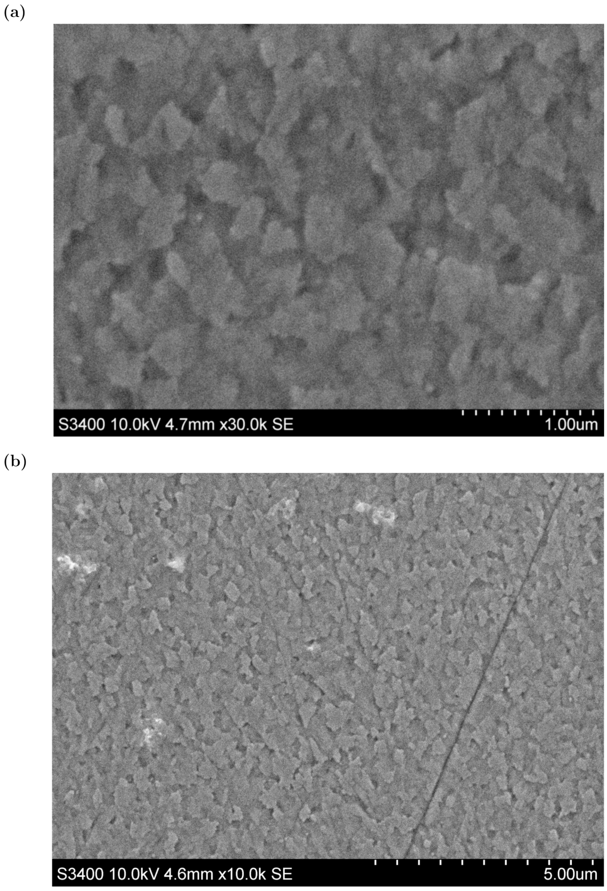

Figure 2. Scanning electron microscopy (SEM) images of the spin-coated pB6CC thin film used in the ITO/pB6CC/Al devices. (a) High-magnification SEM image (30,000×) showing nanoscale granular morphology with a 1 μm scale bar. (b) Lower-magnification SEM image (10,000×) demonstrating uniform film coverage across several microns (5 μm scale bar).

the stochastic switching behavior observed in the memristive devices.

Current–Voltage Characteristics

Memristors inherently exhibit a current–voltage (I–V) relationship dependent on their previous voltage history, making it challenging to determine their baseline direct current (dc) conductivity. Many memristive systems in scientific literature display constantly changing dc I–V curves when the dc voltage is varied within a specific voltage range.[32] An "ideal" memristor, which is never in equilibrium with its source, typically does not exhibit a consistent dc I–V curve.[33,34] Consequently, Figure 3 demonstrates the dc I–V curve for a pB6CC device with sequential voltage variations from 0 to ± 3 V. While the response does not display a classical memory window as seen in binary resistive switching devices, it exhibits analog, history-dependent modulation of current, a hallmark of devices operating in the stochastic regime relevant for synaptic emulation. This form of analog switching is expected for devices intended for spike-timing-dependent plasticity (STDP) and other neuromorphic learning rules, rather than for nonvolatile digital memory. The observed variability is consistent with prior work on soft-matter-based memristors that utilize dynamically reconfigurable percolation pathways, rather than stable filament formation, as the underlying switching mechanism.

The pristine ITO/pB6CC/Al device was subjected to a full cycle of voltage sweeps, consisting of four scans: from 0 V to −3 V (scan 1), − 3 V to 0 V (scan 2), 0 V to +3 V (scan 3), and +3 V to 0 V (scan 4). Figure 3 illustrates the results for multiple cycles, including the first cycle (cf. Figure 3(a)), second cycle (cf. Figure 3(b)), third cycle (cf. Figure 3(c)), and 24th cycle (cf. Figure 3(d)). In scan 1 of the first cycle (0 V to −3 V), the current initially starts at 10^{-8} A, gradually increasing to 10^{-6} A. At −1.2 V, the current sharply rises to 2×10^{-3} A, an approximately 1845-fold increase, indicating a potential "turn-on" event. This elevated current persists through the rest of scan 1, despite significant fluctuations, and reaches a maximum of 10^{-2} A at −3.0 V. Scan 2 (from −3 V to 0 V) shows a relatively smoother trace than scan 1 and more typical of standard resistive behavior. In contrast, scans 3 and 4 (from 0 V to +3 V and +3 V to 0 V, respectively) mirror the elevated current seen in scan 2, but with pronounced scatter and hysteresis in the current readings. Bistable I–V characteristics, like those observed in Figure 3(a), have been documented for various memristive systems, each functioning through varied mechanisms.[8,32]

In the second cycle (cf. Figure 3(b)), the device continues to show elevated current levels following the turn-on event in scan 1. However, the current traces display considerable scatter and pronounced hysteresis between the scans. This hysteretic behavior remains evident in the third cycle (cf. Figure 3(c)) and persists across multiple cycles, as clearly observed in the 24th cycle (cf. Figure 3(d)).

The I–V behavior of the pB6CC memristor unmistakably exhibits strong voltage-history dependence, characterized by a sharp turn-on event, pronounced hysteresis, and the progressive evolution of current across each cycle. In the first scan of the first cycle (cf. Figure 3(a)), the device undergoes a dramatic turn-on at −1.2 V, where the current increases by over 3 orders of magnitude, signaling the onset of a highly conductive state. This transition is not transient but persists across subsequent scans, as evidenced in later cycles (cf. Figure 3(b,c,d)), demonstrating the device's ability to retain and "remember" the voltage that triggered the shift. The observed hysteresis in the I–V curves solidifies this memory effect, where current paths diverge significantly between forward and reverse voltage sweeps. This indicates that the device's conductivity is determined not only by the current applied voltage but also by the sequence of prior voltage exposures, a core trait of memristive systems. As cycling continues, the device further evolves, maintaining elevated current in later cycles, notably in the 24th cycle (cf. Figure 3(d)). The persistent hysteresis and scatter in the current response suggest significant internal changes within the polymer matrix, likely due to charge trapping, local redox changes, or structural rearrangements induced by earlier voltage applications. These behaviors underscore the voltage-history-dependent nature of the polymer memristor, where interactions between internal processes and external voltage follow the fundamental principles of memristive behavior, with the device's current state being shaped by its prior voltage history.

In polymers with both main-chain and pendant carbazole groups (cf. Figure 1), the main-chain carbazoles form a stable percolation network, ensuring consistent charge transport.[35] The pendant carbazole groups, due to their flexibility, establish a dynamic percolation network that is activated by field-induced conformational changes.[20,21] This flexibility allows them to respond dynamically to external stimuli, facilitating

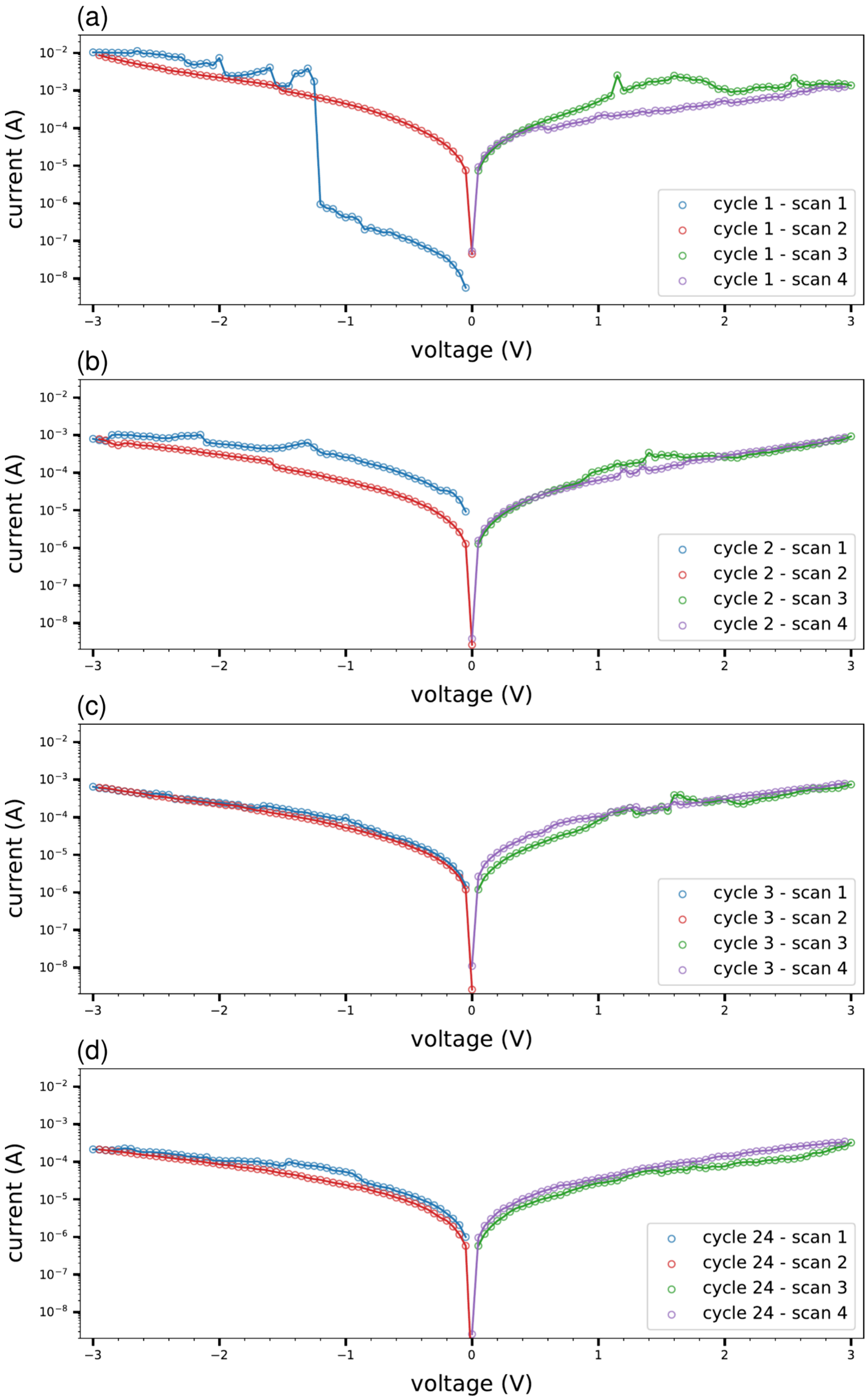

Figure 3. Current response of the pB6CC device to sequential voltage pulses for the (a) 1st cycle, (b) 2nd cycle, (c) 3rd cycle, and (d) 24th cycle. Scans are labeled accordingly. The device structure was ITO/pB6CC/Al.

additional charge transport. However, the well-matched HOMO/LUMO levels between the main-chain and pendant carbazoles play a crucial role in optimizing charge transport. This alignment enables efficient charge transfer not only within the separate networks but also between the main-chain and pendant carbazole units. As a result, the pendant carbazoles not only support charge transport within their network but also contribute to charge movement through the main-chain network, creating a hybrid, interconnected percolation pathway.[17,22,36] The sharp turn-on event can be attributed to the activation of these hybrid percolation pathways, where both main-chain and pendant carbazoles are involved in charge transport. Initially, charge movement is dominated by the main-chain pathways at low voltages. However, as the voltage increases, the pendant carbazoles reorient, activating additional percolation routes and leading to a significant increase in conductivity once a threshold voltage is reached. This behavior mirrors the field-induced ordering seen in similar carbazole-based systems.[22] The hysteresis observed in the *I*−*V* curves is attributed to charge trapping within this hybrid percolation network, aligning with the space-charge-limited current (SCLC) mechanism reported in similar systems.[22] Additionally, the scatter in the data is likely due to variations in the orientation and mobility of both main-chain and pendant carbazole groups under the applied electric field, which affects the overall efficiency of charge transport.

To further establish the reproducibility of this voltage-history-dependent behavior, Figure 4 presents the first four cycle *I*−*V* scans for five representative ITO/pB6CC/Al devices, each fabricated independently under identical conditions. While the precise voltage at which the turn-on event occurs varies between devices, occurring during either the first or second scan of the first cycle, this turn-on event was observed universally across all 14 devices fabricated in this study. Following this turn-on event, a consistent behavioral trend emerges across all devices: the *I*−*V* response undergoes a progressive evolution with each subsequent cycle, reflecting the ongoing charge trapping, local redox changes, and structural rearrangements within the polymer matrix induced by repeated voltage stimulus. Nonetheless, a persistent component of hysteresis between the outward voltage sweep and its return, as clearly illustrated in Figure 3, remains a characteristic feature of the device response across all cycles and all devices, consistent with the space-charge-limited current mechanism discussed above. This cycle-dependent evolution, from an initially stochastic turn-on event toward a more reproducible but persistently hysteretic analog response, is an intrinsic property of the pB6CC material system and was observed across the full ensemble of 14 independently fabricated devices. This reproducibility provides statistical confidence in the volatile, analog switching mechanism that underpins the STDP behavior demonstrated in this work.

To decouple the *I*−*V* response of a pB6CC device from its voltage history, Figure 5 presents the DC *I*−*V* characteristics obtained by applying 10,000 random 180 ms square-wave voltage pulses to a pristine ITO/pB6CC/Al device with no prior voltage exposure. Each pulse amplitude was randomly drawn from a uniform distribution spanning ± 3 V and applied to the aluminum electrode while the ITO contact was grounded. This approach yields a comprehensive mapping of the device's instantaneous current response across the entire voltage range, effectively eliminating memory effects from sequential biasing. The resulting current spans approximately 4 orders of magnitude, from 10^{-8} A to 10^{-4} A, within the ± 3 V window.

For comparison, Figure 5 also presents the response of a standard 100 kΩ resistor subjected to the same randomized excitation sequence. As expected for an Ohmic system, the resistor exhibits a linear and history-independent *I*−*V* trace. Additionally, a structurally related control polymer device (pBC) is shown, which retains the conjugated backbone and ionic side chains of pB6CC but lacks the pendant carbazole group; the structure is presented in Figure 18. This modification replaces the alkyl linker and heteroaromatic substituent with a hydrogen atom, effectively removing the electron-donating and charge delocalization pathways provided by the pendant unit. As a result, the pBC device supports significantly lower current levels, with the measured response reduced by over 2 orders of magnitude across the voltage window compared to the pB6CC device.

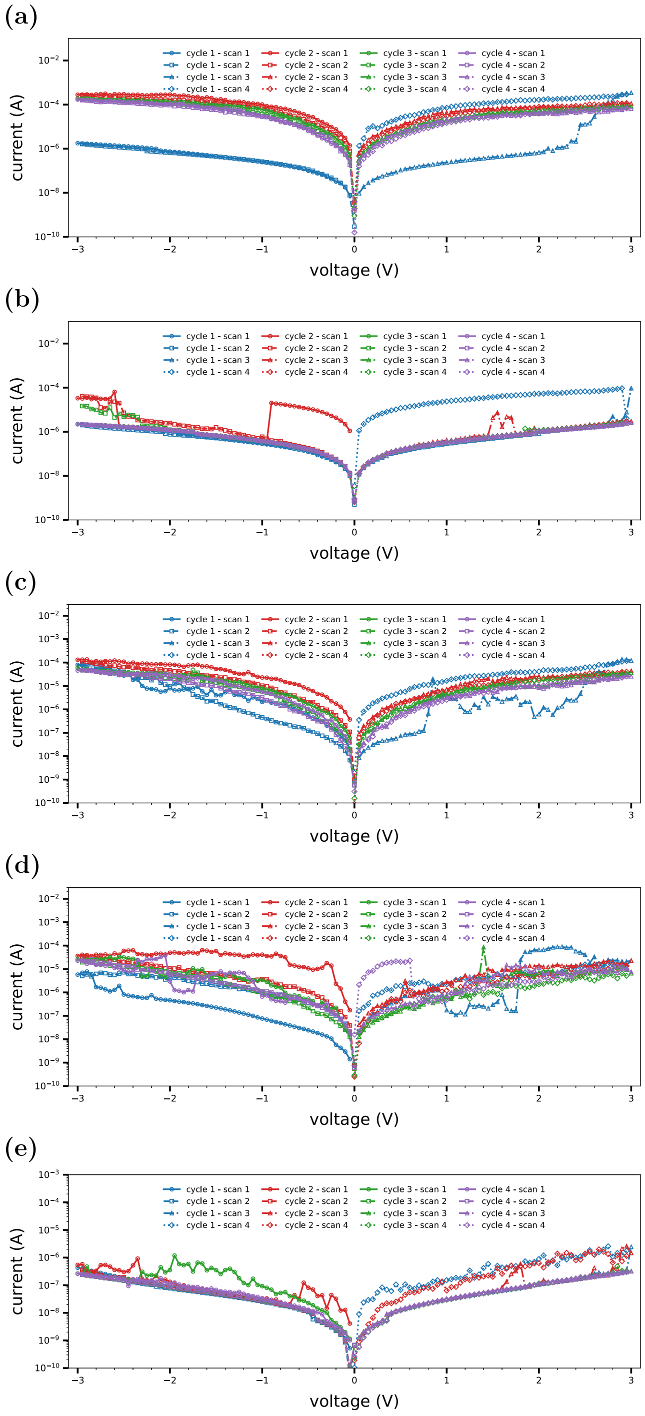

Figure 4. First four cycle *I*−*V* scans for five independently fabricated ITO/pB6CC/Al devices (a−e) showing cycle-dependent hysteretic analog switching behavior.

The randomized *I*−*V* curve for the pB6CC device shows significant variability in current response at a given voltage. For instance, at − 0.05 V, the current ranges from 2.41 nA to 1.18 μA, reflecting a 489-fold difference. In contrast, at 2.95 V, the range is narrower, with current values between 76.3 μA and

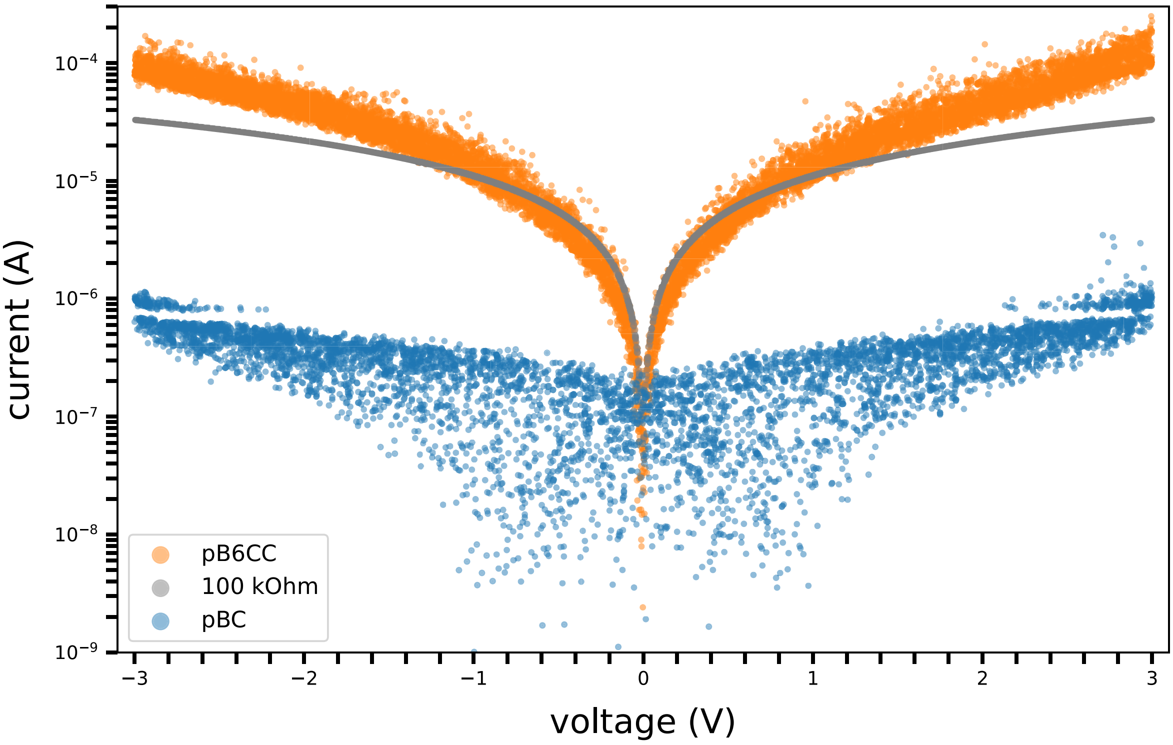

Figure 5. Current response of the pB6CC device (orange) to random excitatory voltage pulses. The device architecture was ITO/pB6CC/Al. For comparison, the response of a 100 kΩ standard resistor (gray) is shown, as well as that of a structurally related control polymer device (pBC, blue). The repeat unit of pB6CC consists of a conjugated carbazole-based backbone with pendant 9-(6-carbazolyl)hexyl substituents and piperidinium sulfonate side chains for ionic solubility. In the pBC variant, the pendant carbazole is removed: the alkyl linker and heteroaromatic unit are replaced with a single hydrogen atom, resulting in a backbone-only system.

249 μA, resulting in a spread of 173 μA. This variability demonstrates the device's differing responses to identical voltage inputs in the randomized protocol. Such broad distributions are in sharp contrast to the more consistent current response seen in the sequential *I*−*V* curve, despite the presence of a turn-on event and hysteresis. The sequential curve shows that the current is heavily influenced by previous voltage exposure. The random *I*−*V* curve, on the other hand, highlights the inherent variability in the device's response without strong voltage history effects.

To quantitatively characterize the volatile nature of the pB6CC memristive device, retention measurements were performed on five independently fabricated ITO/pB6CC/Al devices. Each device was first characterized under open-circuit conditions to establish a prepulse baseline conductance, followed by a programming pulse of −2.0 V applied for 10 s, and subsequently monitored under open-circuit conditions for approximately 600 s postpulse. The results, presented in Figure 6(a) (sample s1 - sample s5), reveal that the programming pulse elevates the device conductance by 10^3−10^5 times above the prepulse baseline, reflecting the stochastic nature of the percolation networks established across independently fabricated devices. Upon removal of the programming field, the conductance decays monotonically in the direction of the prepulse baseline in all devices, confirming the volatile character of the programmed state. The postpulse decay (cf. Figure 6(b)) follows a power law of the form $I/I_{\mathrm{baseline}} = A \cdot t^{-\alpha}$ with an exponent $\alpha = 1.42 \pm 0.14$ ($n = 5$, $R^2 > 0.979$ for all devices). The consistency of α across devices, despite the order-of-magnitude variation in absolute conductance arising from device-to-device differences in film morphology and percolation network topology, which give rise to the probabilistic variation in absolute conductance levels observed across the ensemble, demonstrates that the relaxation dynamics are governed by an intrinsic property of the pB6CC material system rather than by the specific conductive pathways established in any individual device. This power law decay is characteristic of dispersive charge transport in disordered polymer systems, where a broad distribution of trap release times within the carbazole-based percolation network governs the relaxation of both the trapped charge and the associated field-induced conformational states of the pendant carbazole moieties following removal of the programming field. The volatile behavior demonstrated here is not a limitation of the device but rather a defining feature of its intended neuromorphic function, wherein transient synaptic weight modulation, rather than permanent state retention, is the operative mechanism underlying the STDP response presented in a subsequent section.

Inspection of the alignment of the experimentally derived energy levels in the pB6CC device helps illustrate its ability to alter conductivity with voltage pulses. The ITO/pB6CC/Al energy levels, shown in Figure 7, were estimated from UV−vis spectroscopy and cyclic voltammetry, and are used here for qualitative alignment with electrode work functions to explain the observed transport asymmetry and p-type behavior.

For the pB6CC material, Figure 7 indicates that a Schottky barrier forms at the Al/LUMO interface due to the energy gap between the LUMO level (−2.3 eV) and the aluminum electrode's work function (−4.3 eV). Simultaneously, the alignment of the HOMO energy level (−5.1 eV) with the ITO electrode's work function (−4.8 eV) makes ITO a suitable

https://doi.org/10.1021/acsaelm.6c00615
ACS Appl. Electron. Mater. XXXX, XXX, XXX−XXX

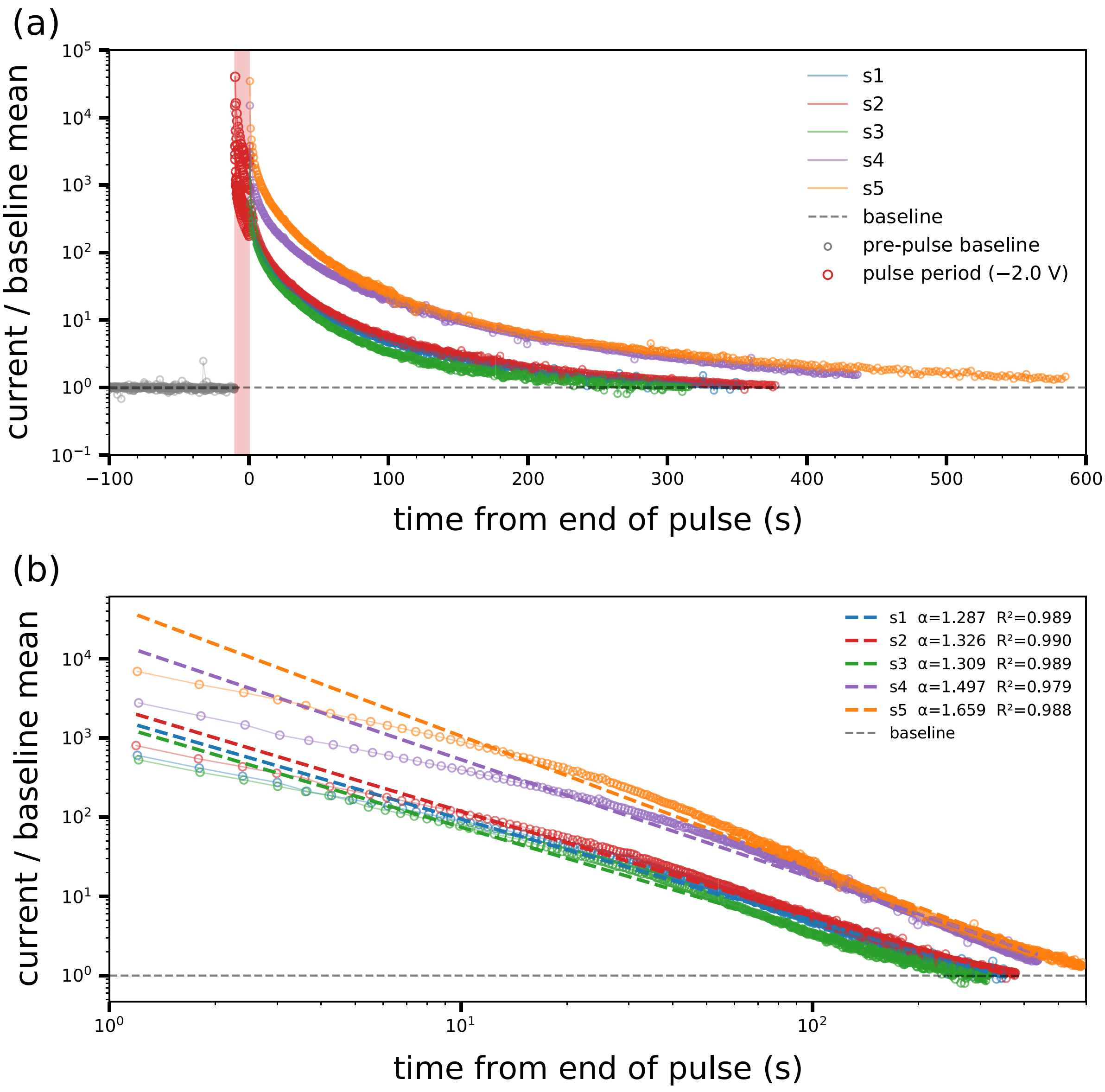

Figure 6. Volatile retention characteristics of ITO/pB6CC/Al devices following a −2.0 V, 10 s programming pulse. (a) Normalized current response (I/I_{baseline}) as a function of time relative to the end of the programming pulse for five independently fabricated devices (sample s1−sample s5). Gray symbols denote the prepulse baseline, red symbols, the under-field current during the programming pulse, and colored symbols, the postpulse decay. The dashed horizontal line indicates the normalized baseline mean. (b) Log−log representation of the postpulse decay overlaid with power law fits ($I/I_{\mathrm{baseline}} = A \cdot t^{-\alpha}$, dashed lines).

choice for a hole-injecting electrode (cf. Figure 7a).[37,38] The turn-on event, observed at −1.2 V during the sequential voltage ramp, is consistent with holes being injected from the ITO into the HOMO level, corroborating the energy alignment discussed earlier. For estimating the LUMO values, the difference between the measured oxidation potential (associated with the HOMO) and the 2.87 eV energy, found at the UV−visible electronic absorption band edge, was utilized.[14]

Spike-Timing-Dependent Plasticity (STDP)

In biological neural networks, spike-timing-dependent plasticity (STDP) serves as an essential mechanism for adaptively adjusting synaptic weights in response to various stimuli, including sensory experiences.[39] STDP has been observed across various regions of the brain, in different animal species, and is considered fundamental to a broad array of cognitive functions such as learning, memory, and attention.[40] Among specific functional consequences theoretically analyzed in the literature are the latency reduction (learning to increase synaptic weight of input neurons that fire early with respect to stimulus onset[41]), learning temporal spike patterns[42] or spatial maps.[43] The dependence of STDP on precise spike timing (on the millisecond scale) allows for tasks such as sound source localization in the auditory pathway,[44] which would be impossible in rate-based learning models.[45] STDP strengthens synapses when a presynaptic spike precedes a postsynaptic one and weakens them otherwise.[46,47]

In artificial intelligence, STDP plays a pivotal role in spiking neural networks (SNNs), setting them apart from traditional artificial neural networks (ANNs) by encoding information through the precise timing of spikes, adding a critical temporal dimension. This, combined with STDP, enhances learning and adaptability while potentially reducing energy consumption

https://doi.org/10.1021/acsaelm.6c00615
ACS Appl. Electron. Mater. XXXX, XXX, XXX−XXX

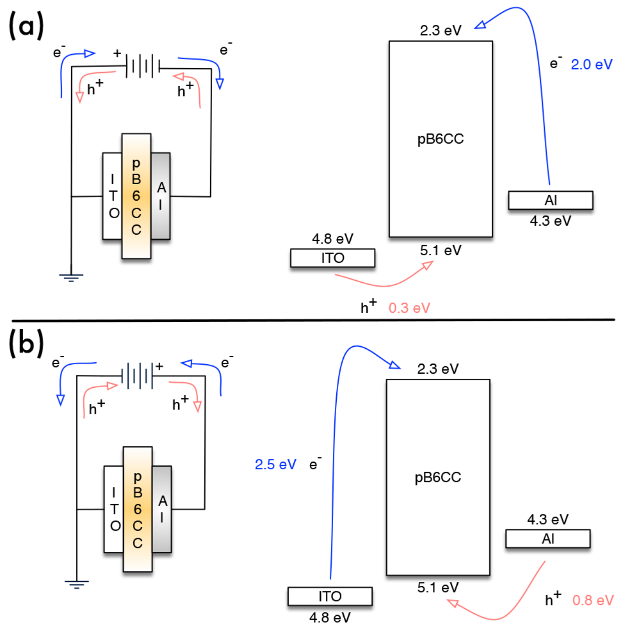

Figure 7. Schematic of charge flow with the ITO electrode tied to the ground and with (a) a negative potential or (b) a positive potential applied to the Al electrode. Electronic characteristics of pB6CC are derived from UV−vis spectroscopy and cyclic voltammetry. Based on the alignment of the HOMO level (−5.1 eV) with the ITO work function (−4.8 eV), hole injection is energetically favorable, indicating that pB6CC behaves predominantly as a p-type semiconductor. The LUMO level lies above the Al work function, consistent with suppressed electron injection. All energies are expressed in eV and are relative to the vacuum level.

compared to ANNs. As a result, SNNs show increased efficiency in tasks such as image and speech recognition.[48] STDP has been extensively explored in various memristive systems.[49,50] Here, our goal is not to implement a full SNN or simulate network-level spike encoding, but rather to demonstrate a synaptic-level learning rule that is foundational to such architectures. Figure 8 illustrates this behavior.

Figure 8a illustrates the STDP current response of an pB6CC device. The experiment consisted of 3000 timing shifts (Δt_s) between the presynaptic and postsynaptic electrodes, uniformly distributed within the range of $|\Delta t_s| \leq 4$ s. Each spike pair consisted of two square-wave pulses at −500 mV with a duration of 60 ms, applied with randomly selected timing separations (Δt_s). After the spike pair, a square-wave measurement pulse of −50 mV with a duration of 60 ms was applied after a delay of 100 ms to evaluate the device's conductivity state by measuring the resulting current. No reset pulse was applied, as the intent was to observe the natural evolution of the device's synaptic weights over time without interruption from a reset mechanism. Additionally, the use of randomized timing shifts (Δt_s) is expected to reduce the net accumulation of synaptic weights, as the random nature of the timing offsets prevents consistent potentiation or depression. The device was allowed to rest for 1 s before the application of the next pulse pair. The average current of 2.5 nA and its standard deviation of 0.2 nA are depicted by the solid and dashed red lines, respectively. Prior to acquiring the data shown in Figure 8a, the device was initialized by applying a −2 V pulse for 1 s to activate it. Details of the turn-on event are provided in the sequential $I-V$ study presented in Figure 3(a). In this study, the aluminum electrode functions as the postsynaptic neuron, while the ITO electrode serves as the presynaptic neuron. The magnitude of the electrical current corresponds to the "synaptic weight" of the connection between these electrodes. As illustrated in Figure 8a, when a presynaptic spike precedes a postsynaptic spike, there is an increase in synaptic strength, a phenomenon known as Long-Term Potentiation (LTP). Conversely, if a presynaptic spike follows a postsynaptic spike, the synaptic strength decreases, a process termed Long-Term Depression (LTD).

Conversely, Figure 8b depicts the STDP behavior of a device composed of ITO/poly(methyl methacrylate) (PMMA)/Al layers. PMMA, when used in such a sandwich configuration, has not been shown to manifest memristive characteristics. Consequently, the device does not display LTP or LTD in its STDP response. For this particular device, the observed currents had an average magnitude of 5.2 nA, with a standard deviation extending across 3 orders of magnitude. This wide variation in current is indicative of the electrically insulative nature of PMMA.

STDP is a prevalent method for adjusting synaptic weights in SNNs. According to the STDP rule, the strength of a synapse is either potentiated or depressed when a presynaptic neuron's spike arrives at a postsynaptic neuron shortly before or after the latter generates a spike, respectively. This modulation in synaptic strength serves as a mechanism for updating the weight function associated with the synapse in question. Specifically, the weight function can be refined based on the magnitude and directionality of the change in synaptic strength, with the objective of optimizing the SNN's performance for a given task. STDP-driven weight alterations are particularly advantageous for tasks that require the learning of complex temporal patterns.

Figure 9 provides a schematic representation of the weight adjustment procedure in an ITO/pB6CC/Al device within the context of a SNN. The methodology for weight modification can differ depending on the specific SNN implementation, but for the current case, weight changes for causal and anticausal spikes are treated distinctly. Causal spikes refer to scenarios where a spike from the presynaptic neuron precedes that of the postsynaptic neuron. Conversely, anticausal spikes occur when a spike from the postsynaptic neuron arrives before that of the presynaptic neuron. By segregating these two types of spike interactions, the weight adjustment process can be more finely tailored to the unique temporal dynamics present within the network.

In this scenario, the spike-timing dependence is assessed using a standard spike pair (SP) with a time difference $\boldsymbol{\Delta t_s}$ between the pre- and postsynaptic neurons (a_{SP}). As shown in Figure 9, the causal spike pair weight update a_c is accumulated as $a_c = a_c + a_{\mathrm{SP}}$. Similarly, if $\Delta t_s < 0$, the anticausal spike pair weight update would also be accumulated.

The accumulated spike-timing dependence can be utilized in weight updates and reset to zero if either spike pair weight update crosses the threshold a_{th} (for instance, $a_c > a_{\mathrm{th}}$). In this case, the reduced symmetric nearest-neighbor spike pairing scheme is implemented instead of considering all past and future spikes; only the most recent and subsequent spike at both synapse terminals are taken into consideration.

To replicate LTP, Figure 10 presents the STDP response of an ITO/pB6CC/Al device, where the timing intervals (Δt_s) between the pre- and postsynaptic electrodes were generated from a normal distribution. Importantly, the distribution's mean ($\mu_{\Delta t}$) and standard deviation ($\sigma_{\Delta t}$) were arbitrarily

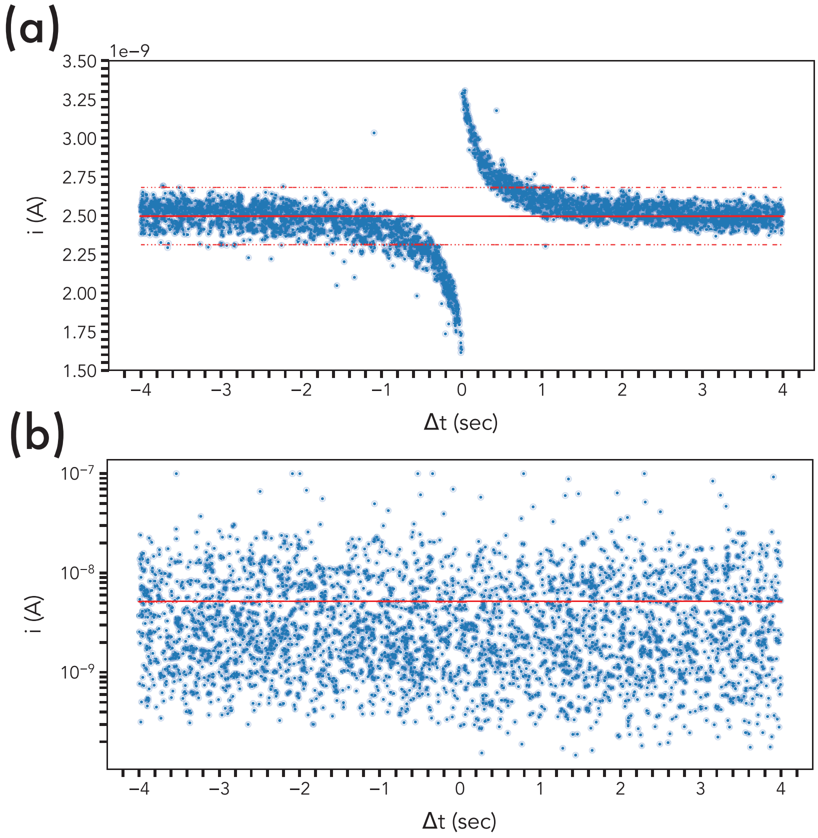

Figure 8. Spike-timing-dependent plasticity (STDP) response of (a) an ITO/pB6CC/Al device and (b) an ITO/PMMA/Al device serving as a nonmemristive baseline control. Red solid and dashed lines indicate the average current and its standard deviation, respectively.

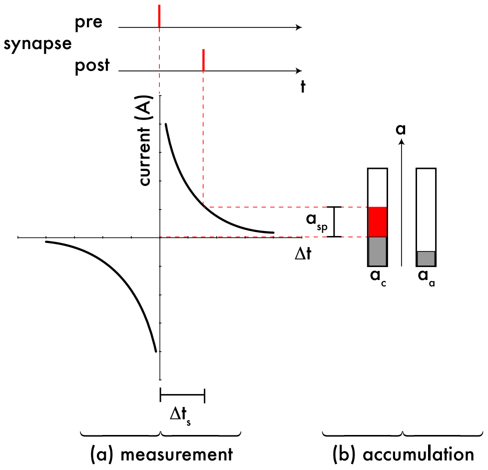

Figure 9. Schematic drawing shows hardware synapses updating weights through a STDP response. The spike-timing-dependence between the pre- and postsynaptic neuron is (a) measured using one standard spike pair with Δt_s and (b) accumulated to a_c in the case of a causal spike pair, while the anticausal spike pair's a_c contribution is not affected.

chosen to be 200 and 300 ms, respectively, to showcase the positive weighting response. Figure 10 presents the mean current response of 2.1 nA and its standard deviation (SD: 0.5 nA), illustrated with solid and dashed red lines, respectively. Because the device operates in a volatile STDP mode without a retention mechanism or permanent weight storage, long-term retention is not the objective of this work.

The readout pulse, with an average current response of 2.1 nA at −50 mV, required 0.105 nW of power and consumed 6.3 pJ of energy. The programming pulse, exhibiting an average current response of 1 μA when applying a −500 mV spike over 60 ms, required 500 nW per pulse. With two such pulses, the total power requirement for the programming phase was 1 μW, and the total energy consumption was 60 nJ. For a complete programming instance, the total power consumption was approximately 1 μW, and the total energy consumption reached 60 nJ. This energy requirement aligns with state-of-the-art memristive systems, which aim to minimize energy consumption while maintaining effective neuromorphic functionality. Recent memristor systems operate under similar low-energy conditions, showcasing memristors with energy consumption values in the tens of nanojoules per operation.[51,52] These systems highlight the ongoing advancements in reducing energy demands in memristor-based neuromorphic computing devices. While this demonstrates the device's effectiveness in simulating synaptic plasticity with relatively low power and energy demands, it remains significantly less energy efficient compared to the human brain. The human brain consumes about 20 W of power for all its functions, corresponding to an estimated energy consumption of approximately 10 fJ to 100 aJ per synaptic event, or a power consumption per synapse on the order of 10 pW to 100 fW.[53]

The discontinuity at $\Delta t_s = 0$ in STDP is crucial for weight updates because it provides a clear distinction between causal and anticausal spike interactions. This distinction is important for capturing the precise timing relationships between pre- and postsynaptic neurons in the network. The probability density distribution of the current response (cf. Figure 11) from Figure

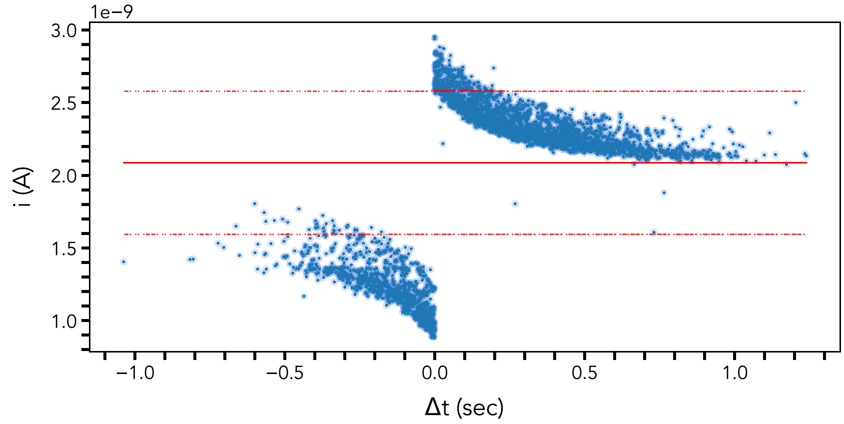

Figure 10. STDP response of the ITO/pB6CC/Al device with average current (red line) of 2.087 × 10^{-09} A (SD: 4.92 × 10^{-10}). Timing (Δt_s) between pre- and postsynaptic electrode sampled from a normal distribution with average and standard deviation of 200 ms and 300 ms, respectively. Red solid and dashed lines are the average and standard deviation of the currents, respectively.

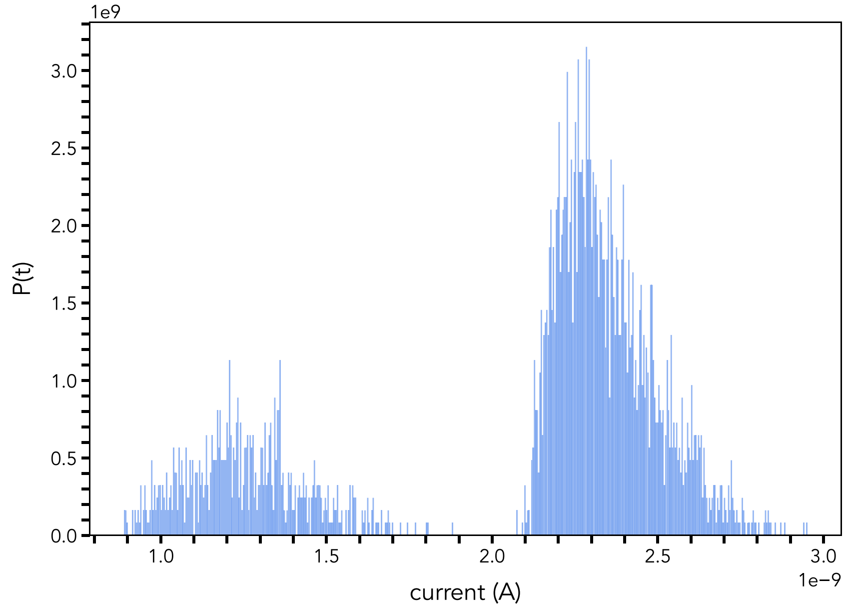

Figure 11. Probability density distribution of the current response of the ITO/pB6CC/Al device to timing shifts (Δt) between the pre- and postsynaptic electrode being sampled from a normal distribution with the mean and standard deviation set to $\mu_{\Delta t}$ = 200 and $\sigma_{\Delta t}$ = 300 ms, respectively. The distribution is based on a sample size of 3000 instances (cf. Figure 10 for the STDP response).

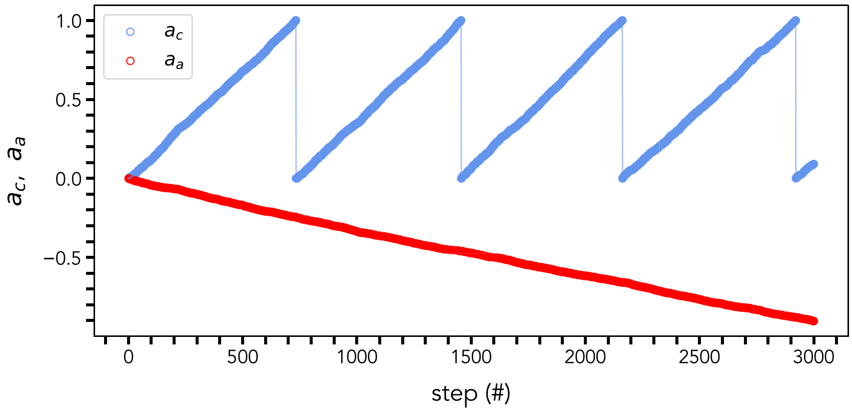

Figure 12. Trajectory of causal and anticausal spike pair weight updates a_c and a_a with 3,000 member sampling of Δt_s from normal distribution with $\mu_{\Delta t}$ = 200 ms and $\sigma_{\Delta t}$ = 300 ms. See Figure 10 for details.

10 highlights the bimodal nature of the current when timing shifts are sampled in the vicinity of Δt_s = 200 ms and indicates a large range of currents from under 1.0 nA to 3 nA.

This discontinuity ensures that the weights are only updated when there is a significant and meaningful temporal relationship between the spikes. Figure 12 presents the causal spike pair weight update a_c and anticausal spike pair weight update a_a for the normal distribution biased sampling of the device presented in Figure 10. Since the normal distribution is centered over 200 ms, the causal spike pair weight updates more frequently than the anticausal spike pair weight update and crosses over the reset threshold of 1 four times within the 3,000-item sampling set. In contrast, the anticausal spike pair weight update never attains a value of −1 and ends the sampling period with a value of −0.903.

Biodegradability Assessment

The emergence of biodegradable or bioresorbable electronics, especially semiconductors susceptible to bacterial degradation, marks a significant advancement in environmental sustainability. Traditional CMOS semiconductors are primarily composed of nonbiodegradable materials, thereby contributing to the escalating problem of electronic waste. Such waste presents not only recycling difficulties but also raises substantial environmental issues, including the risk of landfill accumulation and the leaching of hazardous substances. In contrast, semiconductors capable of bacterial degradation offer an eco-friendly alternative, substantially mitigating the volume of electronic waste and its concomitant environmental repercussions.[54]

Carbazole 1,9a-dioxygenase (CARDO) is a multicomponent enzyme complex originating from the bacterium *Pseudomonas resinovorans* CA10. This complex is known for its ability to degrade carbazole, a heteroaromatic organic molecule that is naturally present in coal tar and serves as a key constituent in the repeat unit of pB6CC (cf. Figure 1).[55−57] The CARDO complex is composed of a ferredoxin (CARDO-F, CarAc protein), a terminal oxygenase (CARDO-O, a homotrimer of CarAa proteins), and a ferredoxin reductase (CARDO-R, a monomer of CarAd protein). These components work in concert to catalyze the dioxygenation of carbazole.[58] The enzymatic action employs molecular oxygen to introduce hydroxyl groups at the 1,9-positions of the carbazole, yielding 1,9-dihydroxy-carbazole. Subsequent metabolic steps further cleave the aromatic ring structure into soluble, low molecular weight compounds such as anthranilic acid, which are readily assimilated by environmental microbes and are not considered toxic.

In the context of pB6CC as illustrated in Figure 1, the degradation mechanisms may target carbazole moieties that are either pendant to the polymer backbone or directly integrated within it, though substrates susceptible to degradation by *P. resinovorans* CA10 appear to be varied and extensive.[56] Importantly, when degradation occurs at the carbazole units situated along the polymer chain, there is a consequent reduction in the molecular weight of the polymer. This diminution in molecular weight facilitates material recyclability, thereby advancing the sustainable management of such polymeric materials.

Although the lysate from *Pseudomonas resinovorans* CA10 can be straightforwardly used for the degradation of carbazole, a more systematic approach for scaling up semiconductor recycling involves utilizing the specific enzymes employed by *Pseudomonas resinovorans* CA10 in carbazole degradation. To achieve this, the CARDO-O, CARDO-F, and CARDO-R proteins, which constitute the CARDO complex, were isolated, purified, and subsequently combined.[59,60] These proteins, along with the *P. resinovorans* CA10 lysate, were used to digest pB6CC.

To assess the effectiveness of degradation, pB6CC was subjected to incubation with both the CARDO enzyme complex and the lysate of *P. resinovorans* CA10, the latter serving as a reference. Figure 13 illustrates the changes in UV/vis absorbance as pB6CC evolves from its monomeric state to a high molecular weight polymer. The absorbance at 425 nm is employed as a robust measure for gauging the polymer's molecular weight. Notably, both the CARDO complex and the cellular lysate displayed minimal absorbance at this wavelength.

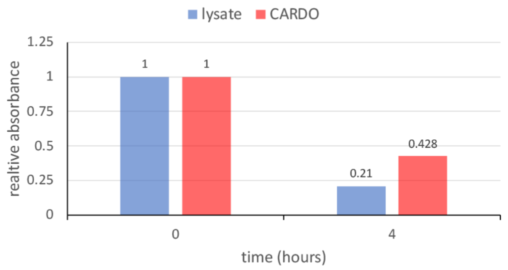

Figure 13. UV/vis absorbance during the polymerization of pB6CC in DMSO (10 μg/mL); polymerization times given in inset.

Figure 14 presents the relative absorbance at 425 nm for pB6CC when incubated with *P. resinovorans* CA10 lysate and the reconstituted CARDO complex. The data reveal that a 4-h incubation at 30 °C with the lysate led to a 79% reduction in absorbance at 425 nm, whereas the CARDO complex resulted in a 57% reduction. Monitoring the decline in absorbance at this specific wavelength serves as an indicator that degradation of the carbazole units is leading to a reduced molecular weight of the polymer. Consequently, both the CARDO complex and the cellular lysate are effective in digesting the polymer.

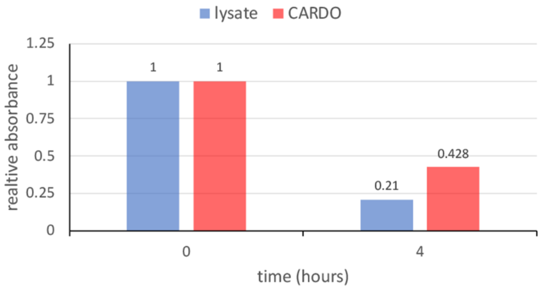

Figure 14. Relative absorbance at 425 nm of pB6CC incubated with *P. resinovorans* CA10 lysate or the reconstituted CARDO complex composed of CARDO-O, CARDO-F, and CARDO-R proteins after 4 h at 30 °C.

To confirm the reduction in molecular weight, thermogravimetric analysis (TGA) was conducted and is presented in Figure 15 and indicates a decreased mass throughout the temperature range for the postdigested polymer variant realtive to the predigested sample. The digestion process breaks down the polymer's long chains into smaller units, which significantly lowers the molecular weight. This decrease plays a crucial role in the more noticeable reduction in the mass of the digested

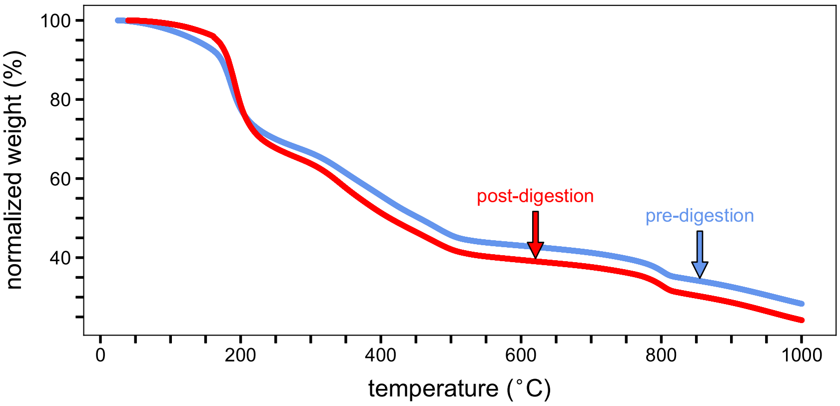

Figure 15. Thermogravimetric analysis (TGA) illustrating the weight reduction profiles of pB6CC before and after its digestion with *P. resinovorans* CA10 lysate.

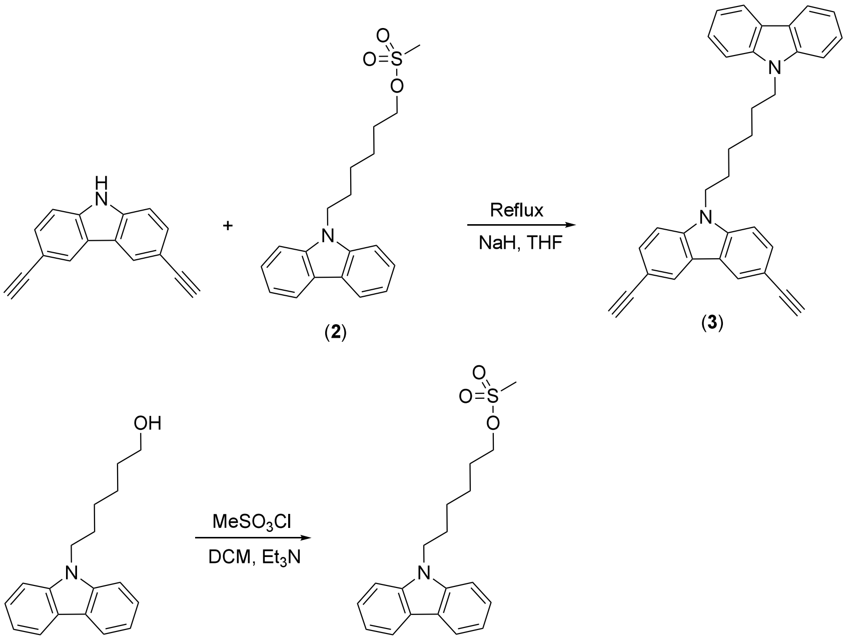

Figure 16. 9-(6-(9*H*-Carbazol-9-yl)hexyl)-3,6-diethynyl-9*H*-carbazole (**3**) synthesis.

polymer compared to the undigested polymer, particularly at the initial temperature of approximately 190 °C. The digestion into smaller, more manageable molecules makes these fragments more volatile, leading to a greater rate of evaporation or degradation as the temperature rises, thus accelerating the weight loss. Furthermore, the digestion process can specifically affect and break down the side chains or branches of the polymer. The modification or removal of these structures not only directly leads to a lower mass but may also change the thermal behavior of the resulting fragments, influencing their stability and volatility. The combination of molecular breakdown, increased volatility of the resulting smaller molecules, and the selective degradation of side structures, results in a more significant weight loss for the digested polymer in comparison to the undigested form.[61]

■ EXPERIMENTAL SECTION

Materials and Methods

All reagents were purchased from Alfa Aesar, TCI America, and used without further purification. All the solvents used for reactions were distilled under argon after drying over an appropriate drying reagent. ^{1}H NMR spectra were recorded on a JEOL ECX−300 spectrometer. Chemical shifts for protons are reported in parts per million downfield from tetramethylsilane and are referenced to residual protium in the NMR solvent ($CDCl_3$: δ 7.26 ppm). High resolution mass analysis was prepared using Waters Q-ToF Premier mass spectrometer. Absorbance spectra was collected using a PerkinElmer Lambda 900 UV−vis/NIR spectrophotometer.

Synthesis

Sodium 3,3′-((2,5-diiodo-1,4-phenylene)bis(oxy))bis(propane-1-sulfonate) (**1**) was synthesized according to the method described in the literature.[62]

6-(9*H*-Carbazol-9-yl)hexan-1-ol was synthesized as described in our previous work.[20]

3,6-Diethynyl-9*H*-carbazole was synthesized following the method from the literature.[63]

6-(9*H*-Carbazol-9-yl)hexyl Methanesulfonate (2) Synthesis. 6-(9*H*-carbazol-9-yl)hexan-1-ol (1 g, 3.74 mmol) and trimethylamine (0.42 g, 4.11 mmol) were dissolved in dichloromethane (15 mL). The solution was cooled to 0 °C, and methanesulfonyl chloride (0.47 g, 4.11 mmol) was added to the cooled stirred solution. The cooling was removed, and the resulting solution was stirred at room temperature for 2 h before being washed with water. The organic layer was separated, dried with Na_2SO_4, filtered, and evaporated under vacuum.

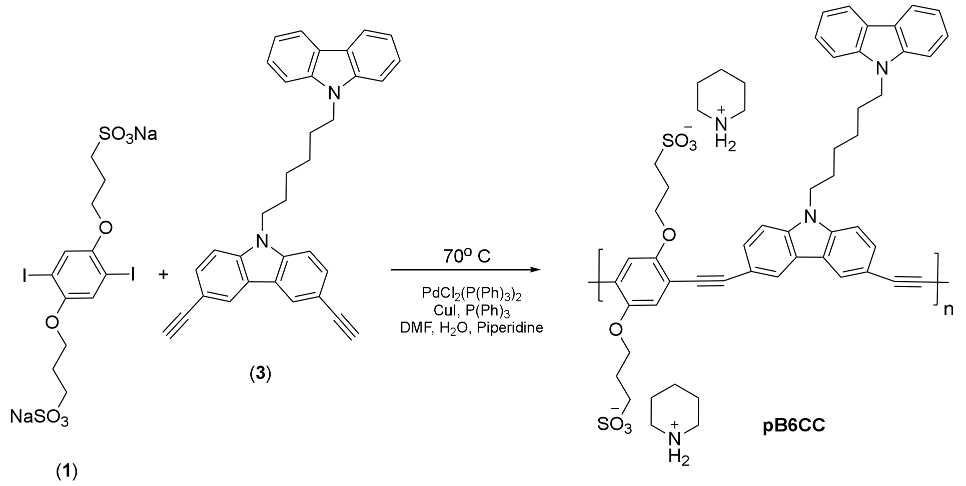

Figure 17. Polymer synthesis (pB6CC).

The obtained clear oil was used in the subsequent step without further purification. Yield: 0.9 g (70%). ^{1}H NMR ($CDCl_3$) δ: 1.42 (m, 4H), 1.69 (m, 2H), 1.91 (m, 2H), 2.93 (s, 3H), 4.16 (t, 2H, J = 6.5 Hz), 4.32 (t, 2H, J = 6.9 Hz), 7.23 (m, 2H, J = 6.9 Hz, J = 1.4 Hz), 7.39 (d, 2H, J = 7.9 Hz), 7.47 (m, 2H, J = 6.9 Hz, J = 1.4 Hz), 8.10 (d, 2H, J = 7.9 Hz).

9-(6-(9*H*-Carbazol-9-yl)hexyl)-3,6-diethynyl-9*H*-carbazole (3) Synthesis. Sodium hydride (0.035 g, 1.46 mmol) was introduced into a stirred solution of 3,6-diethynyl-9*H*-carbazole (0.2 g, 0.93 mmol) in tetrahydrofuran (18 mL) under a nitrogen atmosphere. The mixture was stirred at room temperature for 10 min before adding a solution of 6-(9*H*-carbazol-9-yl)hexyl methanesulfonate (2) (0.35 g, 1.02 mmol) in tetrahydrofuran (2 mL). The resulting mixture was stirred and refluxed under nitrogen for 8 h. After cooling, the mixture was extracted with dichloromethane and washed with water. The organic solution was separated, dried with Na_2SO4, filtered, and evaporated. The crude product was purified by column chromatography on silica using a dichloromethane/hexane (1:2) solvent system, Rf = 0.25. Yield: 0.3 g (69%), clear viscous oil. ^{1}H NMR (CDCl3) δ: 1.34 (m, 4H), 1.80 (m, 4H), 3.08 (s, 2H), 4.18 (t, 2H, J = 6.9 Hz), 4.25 (t, 2H, J = 6.9 Hz), 7.22 (m, 4H, J = 6.9 Hz, J = 8.6 Hz), 7.32 (d, 2H, J = 7.9 Hz), 7.43 (m, 2H, J = 6.9 Hz, J = 1.4 Hz), 7.55 (d.d, J = 8.6 Hz, J = 1.7 Hz), 8.09 (d, 2H, J = 7.9 Hz), 8.20 (d, 2H, J = 1.4 Hz). ESI+ Mass (m/z): calculated for $C34H28N_2$ $[M + H]^+$ 465.225, found 465.230. See Figure 16.

Polymer Synthesis (pB6CC) (4). A solution of sodium 3,3′-((2,5-diiodo-1,4-phenylene)bis(oxy))bis(propane-1-sulfonate)(1) (0.145 g, 0.223 mmol) in water (5 mL) was added to a solution of 9-(6-(9*H*-carbazol-9-yl)hexyl)-3,6-diethynyl-9*H*-carbazole (3) (0.114 g, 0.25 mmol) in dimethylformamide (5 mL) under nitrogen. Subsequently, a solution of $PdCl_2(PPh_3)_2$ (2 mg, 0.003 mmol), CuI (0.8 mg, 0.004 mmol), and PPh_3 (0.6 mg, 0.002 mmol) in piperidine (3 mL) was added to the main mixture of reagents under a nitrogen atmosphere. The resulting mixture was stirred at 70 °C for 20 h. The hot solution was filtered to remove insoluble residual catalyst. After cooling, the mixture was diluted with water (5 mL), and the precipitated polymer was separated by centrifugation. The polymer was dissolved in a minimum of dimethylformamide (2 mL) and precipitated again by the addition of diethyl ether. The obtained solid was centrifuged, washed with water, and dried. Yield: 0.18 g (94%), pale brown-green solid. ^{1}H NMR (DMSO-d_6) δ: 1.35 (br.s, 4H), 1.49 (br,s, 4H), 1.60 (br.s, 8H), 1.73 (br.s, 4H), 2.15 (br.s, 4H), 2.82 (br.s, 4H), 2.96 (br,s, 8H), 4.24 (br.s, 4H), 4.35 (br.s, 4H), 7.19 (m, 4H), 7.45 (m, 2H), 7.55 (m, 2H), 7.66 (br.s, 2H), 8.14 (m, 2H), 8.35 (br.s, 2H), 8.57 (br.s, 2H). During the reaction of polycondensation, piperidinium iodide intermediate reacts with sodium sulfonate groups of the polymer resulting in the formation of sodium iodide and corresponding piperidinium sulfonates. See Figure 17.

Polymer Synthesis (pBC). Polymer (pBC) (cf. Figure 18) was prepared by the same method as for pB6CC using the coupling reaction of 3,6-diethynyl-9*H*-carbazole with compound (1). Yield 98%, pale yellow solid. ^{1}H NMR (DMSO-d_6) δ: 1.40−1.60 (br.s, 12H), 2.15 (m, 4H), 2.79 (m, 4H), 2.95 (m, 8H), 4.21 (br.s, 4H), 7.18 (br.s, 2H), 7.55 (m, 2H), 7.63 (m, 2H), 8.57 (br.s, 2H), 11.82 (br.s, 1H).

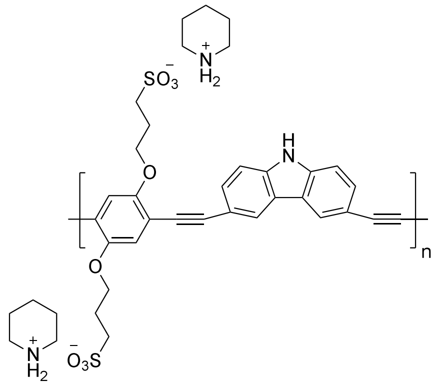

Figure 18. Polymer repeat unit (pBC) composed of piperidinium 3,3′-(1,4-phenylenebis(oxy))bis(propane-1-sulfonate) and 3,6-diethynylcarbazole.

Device Fabrication

Devices were fabricated on unpolished float glass substrates (12.7 mm × 12.7 mm × 0.7 mm) coated on one side with SiO_2 and indium tin oxide (ITO, sheet resistance 8−12 Ω/sq). A 4 mm wide ITO strip was defined by masking with vinyl tape and etching the exposed regions via a zinc/HCl reaction, followed by thorough rinsing and sequential cleaning in acetone and isopropanol with sonication (10 min each). The slides were dried under nitrogen and treated in an oxygen plasma cleaner (Harrick PDC-32G, high setting, 5 min) to remove residual organics and improve surface wettability.

A thin film of pB6CC was deposited by spin coating from a 1:1 water/tetrahydrofuran solution (10 mg/mL) at 2000 rpm. Top electrodes were formed by thermally evaporating aluminum (Kurt J. Lesker pellets, 1/4 in. diameter) in a Denton DV-502A chamber through a shadow mask, producing two crossbar devices per substrate with an active area of 4 mm^2. Deposition was carried out at a base pressure of 2×10^{-6} Torr to a nominal thickness of 200 nm as monitored in situ by a Sigma Instruments SQM-160 thickness controller. The final aluminum thickness was independently verified as 189 nm using a KLA Tencor AlphaStep-IQ profilometer.

The resulting device stack was ITO/pB6CC/Al.

Electrical Characterization

The electrical measurements were conducted using an HP 4156A Semiconductor Parameter Analyzer coupled with an HP 16058A Test Fixture via triaxial leads, all controlled by customized Python code. Unless otherwise specified, the ITO electrode was maintained at zero potential through SMU3, while potentials were applied to the aluminum electrode via SMU1. All measurements were performed at 23 °C unless stated otherwise.

For the randomized $I-V$ response, the device was subjected to voltages ranging from −3 V to +3 V, selected from a uniform distribution. A 180 ms square-wave voltage pulse was applied, and the corresponding current was measured. After each voltage application, the device was grounded through both electrodes for 100 ms before applying the next randomly selected voltage pulse.

For the sequential voltage $I-V$ response, the voltage was ramped from 0 V to ± 3V (or vice versa, depending on the scan) in 50 mV increments. At each voltage step, a 100 ms square-wave pulse was applied at 1.1-s intervals, with the pulse voltage incremented by ± 50 mV. After each voltage application, the device was grounded through both electrodes for 1 s before proceeding to the next step.

Volatile retention characterization was performed on five independently fabricated devices where each measurement consisted of three sequential phases: a prepulse baseline established from 150 read pulses at −50 mV under open-circuit conditions; a −2.0 V programming pulse applied for 10 s with current sampled throughout; and 400 postpulse read pulses at − 50 mV monitoring conductance decay over approximately 600 s. Between all read pulses the device was maintained in an open-circuit state. The stable baseline was determined from the mean of the final 30 prepulse reads. Postpulse decay was fit to a power law $I/I_{\text{baseline}} = A \cdot t^{-\alpha}$ in log−log space.

For spike-timing-dependent plasticity (STDP) measurements, synaptic responses were generated by applying paired presynaptic and postsynaptic spikes. Each spike was defined as a − 500 mV square-wave pulse with a duration of 60 ms. The ITO electrode served as the presynaptic terminal, while the Al electrode was designated as the postsynaptic terminal.

The relative timing shift (Δt_s) between the pre- and postsynaptic spikes was randomly selected from either an uniform or a normal distribution. The uniform distribution spanned − 500 ms to +500 ms, whereas the normal distribution was centered at $\mu = 200$ ms with a standard deviation of $\sigma = 300$ ms. These randomized intervals were chosen to emulate the stochasticity observed in biological synaptic interactions.

Following each spike pair, a − 50 mV square-wave measurement pulse (60 ms duration) was applied 100 ms after the termination of the last spike to probe the updated synaptic weight. Each pulse pair was separated by a 1 s rest period to ensure consistent baseline recovery.

To facilitate data comparison and visualization, responses were normalized relative to a baseline established at $\Delta t_s = 0$. No external reset pulse was applied between trials; instead, the use of randomized Δt_s values inherently limited cumulative weight changes, enabling the observation of intrinsic STDP behavior without interference from residual states.

SEM Characterization

Thin pB6CC films were prepared by spin coating a 10 mg/mL solution in 1:1 (v/v) deionized water/tetrahydrofuran onto ITO-patterned glass substrates at 750 rpm for 40 s, followed by annealing at 105 °C for 3 min and overnight drying under vacuum. SEM imaging was performed using a Hitachi S-3400 variable pressure scanning electron microscope (secondary electron detector, 10 kV accelerating voltage, 30 Pa chamber pressure) with samples mounted on conductive carbon tape and grounded with silver paint.

Pseudomonas resinovorans CA10 Digestion of pB6CC

***P. resinovorans* CA10 Growth.** *P. resinovorans* CA10 was grown in M9 minimal media (47.7 mM Na_2HPO_4, 22 mM KH_2PO_4, 8.5 mM NaCl, 18.7 mM NH_4Cl, 2 mM $MgSO_4$, 0.1 mM $CaCl_2$, and 0.4% glucose) at 32 °C for 24 h with shaking. The cells were harvested using a Beckman Coulter JLA 16.250 rotor at 10,000 x *g* at 4 °C for 20 min. The cell pellet was frozen and stored at −60 °C. The cell paste (5 g) was resuspended in 25 mLs of Buffer A (50 mM Tris-HCl pH 7.5, 1 mM ethylenediaminetetraacetic acid (EDTA), 150 mM KCl, 10% sucrose, 0.01% Igepal, 1 mM benzamide, 10 mg/mL lysozyme, 1 mM phenylmethylsulfonyl fluoride (PMSF) and the protease inhibitors, leupeptin, aprotinin, chymostatin, and pepstatin A at a final concentration of 5 μg/mL). The cells were sonicated with 30 s pulses followed by 15 s rest for 5 min using a sonicator (Qsonica Q125). The lysate was clarified by ultracentrifugation at 40,000 rpm for 90 min in a Beckman Coulter Ti45 rotor at 40,000 rpm at 4 °C. The clarified supernatant was frozen in aliquots and stored at −60 °C.

Degradation of pB6CC with *P. resinovorans* CA10 Lysate. pB6CC (75 μmol) was combined with 0.1 mM NADH and 500 μL of *P. resinovorans* CA10 lysate in Buffer A supplemented with 150 mM KCl, 1 mM dithiothreitol (DTT), and 10% glycerol and incubated at 30 °C for 4 h in the dark. The optical density of the reaction was measured at 425 nm at periodic intervals.

Degradation of pB6CC with CARDO Proteins. The CARDO proteins were expressed and purified as previously described.[59] pB6CC (75 μmol) was combined with 0.1 mM NADH and 10 μmol of each of CARDO-O, CARDO-F, and CARDO-R in 500 μL of Buffer B (50 mM Tris-HCl pH 7.5,

One mM ethylenediaminetetraacetic acid (EDTA), 150 mM KCl, 1 mM dithiothreitol (DTT) and 10% glycerol) and incubated for at 30 °C for 4 h in the dark. The optical density of the reaction was measured at 425 nm at periodic intervals.

Thermogravimetric Analysis of Digested pB6CC. For the digestion of pB6CC with *P. resinovorans* CA10, an incubation solution was prepared containing 0.15 mL of pB6CC in DMSO (100 mg/mL), 0.96 mL of CA10 lysate, 0.24 mL of H_2O, and 0.15 mL of NADH (20 mg/mL), totaling 1.5 mL. The samples were vortexed using a Fisher Scientific Vortex Mixer and incubated in an oven at 40 °C for 24 h. Postincubation, samples were centrifuged using a Thermo Scientific Sorvall Legend Micro 21 Centrifuge at 14,000g for 20 min, after which the supernatant was removed. The samples were subsequently dried in a vacuum oven for at least 48 h.

A TA Instruments Thermogravimetric Analyzer Q5000 was employed with approximately 10 mg of predigested and postdigested pB6CC. The weight loss of each sample was monitored as the temperature was increased from 25 to 1000 °C at a heating rate of 20 °C/min under a nitrogen atmosphere.

■ CONCLUSION

An approach to environmentally sustainable electronics is demonstrated by showcasing a hybrid conjugated polymer, pB6CC, that exhibits spike-timing-dependent plasticity (STDP). This polymer is characterized by its field-sensitive, conformationally flexible pendant carbazole moieties, creating an efficient two-terminal memory device. The unique integration of two independent but synergistic pathways for charge transport enables the achievement of a continuum of resistive states, signifying a major step forward in low-energy analog switching applications. Furthermore, the polymer's biodegradability, facilitated by bacterial degradation, presents an eco-friendly solution to reducing electronic waste, addressing significant environmental concerns associated with the disposal of electronic materials.

Taken together, these results demonstrate the promise of pB6CC as a platform for neuromorphic computing while reinforcing the importance of sustainability in the design of next-generation electronic materials.

AUTHOR INFORMATION

Corresponding Author

Stephen H. Foulger − *Department of Materials Science and Engineering and Department of Bioengineering, Clemson University, Clemson, South Carolina 29634, United States; Center for Optical Materials Science and Engineering Technologies (COMSET), Clemson University, Clemson, South Carolina 29634, United States;* orcid.org/0000-0002-4221-2154; Email: foulger@clemson.edu

Authors

Yuriy Bandera − *Department of Materials Science and Engineering, Clemson University, Clemson, South Carolina 29634, United States; Center for Optical Materials Science and Engineering Technologies (COMSET), Clemson University, Clemson, South Carolina 29634, United States*

Travis Wanless − *Department of Materials Science and Engineering, Clemson University, Clemson, South Carolina 29634, United States*

Igor Luzinov − *Department of Materials Science and Engineering, Clemson University, Clemson, South Carolina 29634, United States; Center for Optical Materials Science and Engineering Technologies (COMSET), Clemson University, Clemson, South Carolina 29634, United States;* orcid.org/0000-0002-1604-6519

Olivia Cobb − *Department of Genetics and Biochemistry, Clemson University, Clemson, South Carolina 29634, United States*

Michael G. Sehorn − *Department of Genetics and Biochemistry, Clemson University, Clemson, South Carolina 29634, United States; Center for Optical Materials Science and Engineering Technologies (COMSET), Clemson University, Clemson, South Carolina 29634, United States*

Lubomir Kostal − *Institute of Physiology, Computational Neuroscience Group, Czech Academy of Sciences, 142 20 Prague 4, Czech Republic*

Jiří Pfleger − *Otto Wichterle Centre of Polymer Materials and Technologies, Institute of Macromolecular Chemistry, 162 06 Prague 6, Czech Republic;* orcid.org/0000-0001-9576-7551

Jarmila Vilčáková − *Department of Physics and Materials Engineering, Faculty of Technology, Tomas Bata University in Zlín, 760 01 Zlín, Czech Republic;* orcid.org/0000-0002-1216-2862

Complete contact information is available at: https://pubs.acs.org/10.1021/acsaelm.6c00615

Notes

The authors declare no competing financial interest.

ACKNOWLEDGMENTS

The authors thank the Gregg-Graniteville Foundation, the National Science Foundation (OIA-1632881 & OIA-1655740), the Ministry of Education, Youth and Sports of the Czech Republic (the Program INTER-EXCELLENCE, LUAUS24032), and DKRVO (RP/CPS/2022/005) for financial support.

REFERENCES

(1) Roy, K.; Jaiswal, A.; Panda, P. Towards spike-based machine intelligence with neuromorphic computing. *Nature* **2019**, *575*, 607−617.

(2) Furber, S. B.; Galluppi, F.; Temple, S.; Plana, L. A. The SpiNNaker Project. *Proceedings of the Ieee* **2014**, *102*, 652−665.

(3) Jo, S. H.; Chang, T.; Ebong, I.; Bhadviya, B. B.; Mazumder, P.; Lu, W. Nanoscale Memristor Device as Synapse in Neuromorphic Systems. *Nano Lett.* **2010**, *10*, 1297−1301.

(4) Akopyan, F.; et al. True North: Design and Tool Flow of a 65 mW 1 Million Neuron Programmable Neurosynaptic Chip. *Ieee Transactions on Computer-Aided Design of Integrated Circuits and Systems* **2015**, *34*, 1537−1557.

(5) Davies, M.; et al. Loihi: A Neuromorphic Manycore Processor with On-Chip Learning. *IEEE Micro* **2018**, *38*, 82−99.

(6) Liu, H.; Qin, Y.; Chen, H.-Y.; Wu, J.; Ma, J.; Du, Z.; Wang, N.; Zou, J.; Lin, S.; Zhang, X.; Zhang, Y.; Wang, H. Artificial Neuronal Devices Based on Emerging Materials: Neuronal Dynamics and Applications. *Adv. Mater.* **2023**, *35*, 2205047.

(7) Chen, W.; Song, L.; Wang, S.; Zhang, Z.; Wang, G.; Hu, G.; Gao, S. Essential Characteristics of Memristors for Neuromorphic Computing. *Advanced Electronic Materials* **2023**, *9*, 2200833.

(8) Chen, Y.; Liu, G.; Wang, C.; Zhang, W. B.; Li, R. W.; Wang, L. X. Polymer memristor for information storage and neuromorphic applications. *Materials Horizons* **2014**, *1*, 489−506.

(9) Wang, Z. Y.; Wang, L. Y.; Nagai, M.; Xie, L. H.; Yi, M. D.; Huang, W. Nanoionics-Enabled Memristive Devices: Strategies and Materials for Neuromorphic Applications. *Advanced Electronic Materials* **2017**, *3*, 1600510.

(10) Jaafar, A. H.; O'Neill, M.; Kelly, S. M.; Verrelli, E.; Kemp, N. T. Percolation Threshold Enables Optical Resistive-Memory Switching and Light-Tuneable Synaptic Learning in Segregated Nanocomposites. *Advanced Electronic Materials* **2019**, *5*, 1900197.

(11) Kirkpatrick, S. Percolation and Conduction. *Rev. Mod. Phys.* **1973**, *45*, 574−588.

(12) Ries, B.; Bassler, H.; Silver, M. PSEUDO-PERCOLATION OF CHARGE-CARRIERS IN MOLECULARLY DOPED POLYMERS - A MONTE-CARLO STUDY. *Philosophical Magazine B-Physics of Condensed Matter Statistical Mechanics Electronic Optical and Magnetic Properties* **1986**, *54*, 141−155.

(13) Foulger, S. H. Reduced percolation thresholds of immiscible conductive blends. *J. Polym. Sci., Part B: Polym. Phys.* **1999**, *37*, 1899−1910.

(14) Foulger, S. H.; Bandera, Y.; Grant, B.; Vilčáková, J.; Sáha, P. Exploiting multiple percolation in two-terminal memristor to achieve a multitude of resistive states. *Journal of Materials Chemistry C* **2021**, *9*, 8975−8986.

(15) Zhao, X. Y.; Pinto, M. R.; Hardison, L. M.; Mwaura, J.; Muller, J.; Jiang, H.; Witker, D.; Kleiman, V. D.; Reynolds, J. R.; Schanze, K. S. Variable band gap poly(arylene ethynylene) conjugated polyelectrolytes. *Macromolecules* **2006**, *39*, 6355−6366.

(16) Jiang, H.; Zhao, X. Y.; Shelton, A. H.; Lee, S. H.; Reynolds, J. R.; Schanze, K. S. Variable-Band-Gap Poly(arylene ethynylene) Conjugated Polyelectrolytes Adsorbed on Nanocrystalline TiO2: Photocurrent Efficiency as a Function of the Band Gap. *ACS Appl. Mater. Interfaces* **2009**, *1*, 381−387.

(17) Lim, S. L.; Ling, Q. D.; Teo, E. Y. H.; Zhu, C. X.; Chan, D. S. H.; Kang, E. T.; Neoh, K. G. Conformation-induced electrical bistability in non-conjugated polymers with pendant carbazole moieties. *Chem. Mater.* **2007**, *19*, 5148−5157.

(18) Fang, Y. K.; Liu, C. L.; Chen, W. C. New random copolymers with pendant carbazole donor and 1,3,4-oxadiazole acceptor for high performance memory device applications. *J. Mater. Chem.* **2011**, *21*, 4778−4786.

(19) Liu, G.; Zhang, B.; Chen, Y.; Zhu, C. X.; Zeng, L. J.; Chan, D. S. H.; Neoh, K. G.; Chen, J. N.; Kang, E. T. Electrical conductivity switching and memory effects in poly(N-vinylcarbazole) derivatives with pendant azobenzene chromophores and terminal electron acceptor moieties. *J. Mater. Chem.* **2011**, *21*, 6027−6033.

(20) McFarlane, T. M.; Zdyrko, B.; Bandera, Y.; Worley, D.; Klep, O.; Jurca, M.; Tonkin, C.; Foulger, S. H.; Vilcakova, J.; Saha, P.; Pfleger, J. Design rules for carbazole derivatized n-alkyl methacrylate

polymeric memristors. *Journal of Materials Chemistry C* **2018**, *6*, 2533−2545.

(21) McFarlane, T.; Bandera, Y.; Grant, B.; Zdyrko, B.; Foulger, S. H.; Vilcakova, J.; Saha, P.; Pfleger, J. Carbazole Derivatized n-Alkyl Methacrylate Polymeric Memristors as Flexible Synaptic Substitutes. *Advanced Electronic Materials* **2020**, *6*, 2000042.

(22) Liu, G.; Liaw, D. J.; Lee, W. Y.; Ling, Q. D.; Zhu, C. X.; Chan, D. S. H.; Kang, E. T.; Neoh, K. G. Tristable electrical conductivity switching in a polyfluorene-diphenylpyridine copolymer with pendant carbazole groups. *Philosophical Transactions of the Royal Society a-Mathematical Physical and Engineering Sciences* **2009**, *367*, 4203−4214.

(23) Zhang, B.; Liu, Y. L.; Chen, Y.; Neoh, K. G.; Li, Y. X.; Zhu, C. X.; Tok, E. S.; Kang, E. T. Nonvolatile Rewritable Memory Effects in Graphene Oxide Functionalized by Conjugated Polymer Containing Fluorene and Carbazole Units. *Chem.—Eur. J.* **2011**, *17*, 10304−10311.

(24) Park, S.; Lee, T. J.; Kim, D. M.; Kim, J. C.; Kim, K.; Kwon, W.; Ko, Y. G.; Choi, H.; Chang, T.; Ree, M. Electrical Memory Characteristics of a Nondoped pi-Conjugated Polymer Bearing Carbazole Moieties. *J. Phys. Chem. B* **2010**, *114*, 10294−10301.

(25) Hahm, S. G.; Kang, N. G.; Kwon, W.; Kim, K.; Ko, Y. G.; Ahn, S.; Kang, B. G.; Chang, T.; Lee, J. S.; Ree, M. Programmable Bipolar and Unipolar Nonvolatile Memory Devices Based on Poly(2-(N-carbazolyl)ethyl methacrylate) End-Capped with Fullerene. *Adv. Mater.* **2012**, *24*, 1062−1066.

(26) Hota, M. K.; Bera, M. K.; Kundu, B.; Kundu, S. C.; Maiti, C. K. A Natural Silk Fibroin Protein-Based Transparent Bio-Memristor. *Adv. Funct. Mater.* **2012**, *22*, 4493−4499.

(27) Park, Y.; Lee, J.-S. Artificial Synapses with Short- and Long-Term Memory for Spiking Neural Networks Based on Renewable Materials. *ACS Nano* **2017**, *11*, 8962−8969.

(28) Xing, Y.; Shi, C.; Zhao, J.; Qiu, W.; Lin, N.; Wang, J.; Yan, X. B.; Yu, W. D.; Liu, X. Y. Mesoscopic-Functionalization of Silk Fibroin with Gold Nanoclusters Mediated by Keratin and Bioinspired Silk Synapse. *Small* **2017**, *13*, 1702390.

(29) Qi, Y.; Sun, B.; Fu, G.; Li, T.; Zhu, S.; Zheng, L.; Mao, S.; Kan, X.; Lei, M.; Chen, Y. A nonvolatile organic resistive switching memory based on lotus leaves. *Chem. Phys.* **2019**, *516*, 168−174.

(30) Dang, B.; Wu, Q.; Song, F.; Sun, J.; Yang, M.; Ma, X.; Wang, H.; Hao, Y. A bio-inspired physically transient/biodegradable synapse for security neuromorphic computing based on memristors. *Nanoscale* **2018**, *10*, 20089−20095.

(31) Oh, S.; Kim, H.; Kim, S. E.; Kim, M.-H.; Park, H.-L.; Lee, S.-H. Biodegradable and Flexible Polymer-Based Memristor Possessing Optimized Synaptic Plasticity for Eco-Friendly Wearable Neural Networks with High Energy Efficiency. *Advanced Intelligent Systems* **2023**, *5*, 2200272.

(32) Cho, B.; Song, S.; Ji, Y.; Kim, T. W.; Lee, T. Organic Resistive Memory Devices: Performance Enhancement, Integration, and Advanced Architectures. *Adv. Funct. Mater.* **2011**, *21*, 2806−2829.

(33) Chua, L. O. Missing Circuit Element. *IEEE Transactions on Circuit Theory* **1971**, *18*, 507−519.

(34) Chua, L. If it's pinched it's a memristor. *Semicond. Sci. Technol.* **2014**, *29*, 104001.

(35) Yen, H. J.; Shan, C. S.; Wang, L.; Xu, P.; Zhou, M.; Wang, H. L. Development of Conjugated Polymers for Memory Device Applications. *Polymers* **2017**, *9*, 25.

(36) Oshima, R.; Biswas, M.; Wada, T.; Uryu, T. HOLE TRANSPORT PROPERTY OF POLY(2-N-CARBAZOLYLETHYL METHACRYLATE). *Journal of Polymer Science Part C-Polymer Letters* **1985**, *23*, 151−154.

(37) Kim, J. S.; Granstrom, M.; Friend, R. H.; Johansson, N.; Salaneck, W. R.; Daik, R.; Feast, W. J.; Cacialli, F. Indium-tin oxide treatments for single- and double-layer polymeric light-emitting diodes: The relation between the anode physical, chemical, and morphological properties and the device performance. *J. Appl. Phys.* **1998**, *84*, 6859−6870.

(38) Ling, Q. D.; Song, Y.; Lim, S. L.; Teo, E. Y. H.; Tan, Y. P.; Zhu, C. X.; Chan, D. S. H.; Kwong, D. L.; Kang, E. T.; Neoh, K. G. A dynamic random access memory based on a conjugated copolymer containing electron-donor and -acceptor moieties. *Angew. Chem., Int. Ed.* **2006**, *45*, 2947−2951.

(39) Gerstner, W.; Kistler, W. M.; Naud, R.; Paninski, L. *Neuronal dynamics: From single neurons to networks and models of cognition*; Cambridge University Press: Cambridge, 2014.

(40) Abbott, L. F.; Nelson, S. B. Synaptic plasticity: taming the beast. *Nat. Neurosci.* **2000**, *3*, 1178−1183.

(41) Song, S.; Miller, K. D.; Abbott, L. F. Competitive Hebbian learning through spike-timing-dependent synaptic plasticity. *Nat. Neurosci.* **2000**, *3*, 919−926.

(42) Gerstner, W.; Ritz, R.; van Hemmen, J. L. Why spikes? Hebbian learning and retrieval of time-resolved excitation patterns. *Biol. Cybern.* **1993**, *69*, 503−515.

(43) Kremer, Y.; Leger, J.-F.; Goodman, D.; Brette, R.; Bourdieu, L. Late Emergence of the Vibrissa Direction Selectivity Map in the Rat Barrel Cortex. *J. Neurosci.* **2011**, *31*, 10689−10700.

(44) Gerstner, W.; Kempter, R.; van Hemmen, J. L.; Wagner, H. A neuronal learning rule for sub-millisecond temporal coding. *Nature* **1996**, *383*, 76−78.

(45) Kempter, R.; Gerstner, W.; van Hemmen, J. L. Hebbian learning and spiking neurons. *Phys. Rev. E* **1999**, *59*, 4498−4514.

(46) Abbott, L. F.; Regehr, W. G. Synaptic computation. *Nature* **2004**, *431*, 796−803.

(47) Bi, G.; Poo, M. Synaptic modifications in cultured hippocampal neurons: Dependence on spike timing, synaptic strength, and postsynaptic cell type. *J. Neurosci.* **1998**, *18*, 10464−10472.

(48) Merolla, P. A.; et al. A million spiking-neuron integrated circuit with a scalable communication network and interface. *Science* **2014**, *345*, 668−673.

(49) Serrano-Gotarredona, T.; Masquelier, T.; Prodromakis, T.; Indiveri, G.; Linares-Barranco, B. STDP and STDP variations with memristors for spiking neuromorphic learning systems. *Frontiers in Neuroscience* **2013**, *7*, 1.

(50) Indiveri, G.; Liu, S.-C. Memory and Information Processing in Neuromorphic Systems. *Proceedings of the Ieee* **2015**, *103*, 1379−1397.

(51) Guo, T.; Pan, K.; Jiao, Y.; Sun, B.; Du, C.; Mills, J. P.; Chen, Z.; Zhao, X.; Wei, L.; Zhou, Y. N.; Wu, Y. A. Versatile memristor for memory and neuromorphic computing. *Nanoscale Horiz* **2022**, *7*, 299−310.

(52) Meng, Y.; Zhu, J. Low energy consumption fiber-type memristor array with integrated sensing-memory. *Nanoscale Adv.* **2022**, *4*, 1098−1104.

(53) Raichle, M. E.; Mintun, M. A. Brain work and brain imaging. *Annu. Rev. Neurosci.* **2006**, *29*, 449−76.

(54) Feig, V. R.; Tran, H.; Bao, Z. N. Biodegradable Polymeric Materials in Degradable Electronic Devices. *Acs Central Science* **2018**, *4*, 337−348.

(55) Ouchiyama, N.; Zhang, Y.; Omori, T.; Kodama, T. BIODEGRADATION OF CARBAZOLE BY PSEUDOMONAS SPP CA06 AND CA10. *Biosci., Biotechnol., Biochem.* **1993**, *57*, 455−460.

(56) Nojiri, H.; Nam, J. W.; Kosaka, M.; Morii, K. I.; Takemura, T.; Furihata, K.; Yamane, H.; Omori, T. Diverse oxygenations catalyzed by carbazole 1,9a-dioxygenase from Pseudomonas sp strain CA10. *J. Bacteriol.* **1999**, *181*, 3105−3113.

(57) Sato, S.; Ouchiyama, N.; Kimura, T.; Nojiri, H.; Yamane, H.; Omori, T. Cloning of genes involved in carbazole degradation of Pseudomonas sp. strain CA10: Nucleotide sequences of genes and characterization of meta-cleavage enzymes and hydrolase. *J. Bacteriol.* **1997**, *179*, 4841−4849.

(58) Nojiri, H.; Habe, H.; Omori, T. Bacterial degradation of aromatic compounds via angular dioxygenation. *Journal of General and Applied Microbiology* **2001**, *47*, 279−305.

(59) Daniele, M. A.; Bandera, Y. P.; Foulger, S. H. Manipulation of Forster Energy Transfer of Coupled Fluorophores Through Biotransformation by Pseudomonas resinovorans CA10. *Photochem. Photobiol.* **2012**, *88*, 129−134.

(60) Daniele, M. A.; Bandera, Y. P.; Sharma, D.; Rungta, P.; Roeder, R.; Sehorn, M. G.; Foulger, S. H. Substrate-Baited Nanoparticles: A Catch and Release Strategy for Enzyme Recognition and Harvesting. *Small* **2012**, *8*, 2083−2090.

(61) Ruggero, F.; Carretti, E.; Gori, R.; Lotti, T.; Lubello, C. Monitoring of degradation of starch-based biopolymer film under different composting conditions, using TGA, FTIR and SEM analysis. *Chemosphere* **2020**, *246*, 125770.

(62) Xie, D.; Parthasarathy, A.; Schanze, K. S. Aggregation-induced amplified quenching in conjugated polyelectrolytes with interrupted conjugation. *Langmuir* **2011**, *27*, 11732−6.

(63) Shanmugaraju, S.; Bar, A. K.; Chi, K.-W.; Mukherjee, P. S. Coordination-Driven Self-Assembly of Metallamacrocycles via a New PtII2 Organometallic Building Block with 90° Geometry and Optical Sensing of Anions. *Organometallics* **2010**, *29*, 2971−2980.

https://doi.org/10.1021/acsaelm.6c00615